nanomaterials

MDPI

Type of the Paper: Article

Observation of multi-phonon emission in 1L WS_2 on various substrates

Eli R. Adler [1,2*], Thy Doan Mai Le [1] , Ibrahim Boulares [2], Robert Boyd [3], Yangchen He
Daniel Rhodes [3], Edward Van Keuren [1], Paola Barbara [1*], and Sina Najmaei [2,*]

[1] Georgetown University, Department of Physics, Washington DC 20057
[2] Army Research Directorate, DEVCOM Army Research Laboratory, Adelphi, Maryland 20783, USA

[3] Department of Materials Science and Engineering, University of Wisconsin, Madison, WI, USA.

* Correspondence: Paola.Barbara@georgetown.edu (PB), sina.najmaei.civ@army.mil (SM).

Abstract: Transition metal dichalcogenides (TMDs) have unique absorption and emission properties that stem from their large excitonic binding energies, reduced-dielectric screening, and strong spin-orbit coupling. However, the role of substrates, phonons, and material defects in the excitonic scattering processes remains elusive. In tungsten-based TMDs, it is known that the excitons formed from electrons in the lower-energy conduction bands are dark in nature, while low-energy emissions in the photoluminescence spectrum have been linked to the brightening of these transitions, either via defect scattering or via phonon scattering with 1st-order phonon replicas. Through temperature and incident-power-dependent studies of WS_2 grown by CVD or exfoliated from high-purity bulk crystal on different substrates, we demonstrate that the strong exciton-phonon coupling yields brightening of dark transitions up to 6th order phonon replicas. We discuss the critical role of defects in the brightening pathways of dark excitons and their phonon replicas and we elucidate that these emissions are intrinsic to the material and independent of substrate, encapsulation, growth method, and transfer approach.

Keywords: keyword 1; keyword 2; keyword 3 (List three to ten pertinent keywords specific to the article yet reasonably common within the subject discipline.)

1. Introduction

The very intriguing electronic structure of monolayer transition metal dichalcogenides (TMDs) arises from the strong spin-orbit coupling and the lack of inversion symmetry, yielding a spin-splitting of the conduction and the valence bands at the K and K' valleys of the hexagonal Brillouin zone, where the extrema of their direct bandgaps are located**[1, 2]**. Such properties are unique to these materials and open exciting pathways towards novel spin/valley opto-electronics applications**[3]**, especially in the realm of quantum computation**[4, 5]**. However, such applications require a thorough understanding of the complex optical excitation and relaxation processes in these two-dimensional semiconductors. There are a variety of monolayer semiconducting TMDs (MX_2, with M = Mo, W and X = S, Se and Te), with important differences in their optical transitions. Unlike molybdenum-based TMDs, the lower conduction band in tungsten-based TMDs carries an opposite spin to that of the upper valence band, making these lower energy, intra-valley transitions spin-forbidden. There are also momentum-forbidden transitions between conduction and valence bands with the same spin, but in different valleys. Nevertheless, in addition to the optically-allowed bright transitions (e.g. neutral excitons and trions), the emission characteristics of monolayer tungsten-based TMDs show an increased level of

Citation: To be added by editorial staff during production.

Academic Editor: Firstname Lastname

Received: date
Revised: date
Accepted: date
Published: date

complexity at lower energies, with a plethora of emissions that are not yet fully understood. These low-energy emissions have been broadly attributed to the brightening of initially dark excitons, either via defect or phonon scattering. Elastic scattering and binding by defects brighten these dark transitions by providing the spin-flip or the momentum change required by the selection rules, without the need of phonons[6-9]. This process gives rise to zero-phonon-line emissions, namely emissions with no phonon scattering.[10-13] Inelastic scattering with phonons, however, results in emissions that are replicas of the zero-phonon lines at energies shifted by an integer value of the phonon's energy [10-14]. The strength of the electron-phonon coupling determines the specific phonons involved in the brightening of dark excitons[13]. Several emissions linked to inelastic scattering with phonons have been observed, including spin-flipping Γ phonons and spin-conserving K or Λ phonons [11-13, 15]. In all cases, the emissions were attributed to first-order replicas, corresponding to single-phonon emissions.

It is clear that defects play an important role in the brightening of these dark excitons, but so far the identities of the types of defects involved in the scattering process have been elusive. Recent studies included magneto-photoluminescence, resonant Raman, and photoluminescence spectroscopy on high-quality WS_2 or WSe_2 exfoliated from bulk crystals and, in some cases, encapsulated in hexagonal boron nitride (hBN) **[10-13, 15, 16]**. Even very clean samples, such as those encapsulated in hBN, have been argued to have defects that were intrinsic to the material, but could not be attributed to specific vacancies, therefore questions on their origin have been left open**[11]**. The picture becomes more complicated for defects in larger-area materials grown by chemical vapor deposition (CVD) and for substrates other than hBN. The presence of substrate non-uniformity, as well as of the impurities left from the transfer process, may play a significant role in the brightening of dark excitons, but systematic studies on the effect of the defect density in the material, of the encapsulation and of the interaction with the substrate are still lacking.

In this work, we present temperature, incident-power and polarization-dependent photoluminescence (PL) measurements on monolayer TMD flakes that are suspended or supported by a substrate. Specifically, we studied WS_2 that was a) exfoliated and encapsulated on hBN, b) directly grown by chemical vapor deposition (CVD) on hBN and SiO_2, and c) grown by CVD and transferred onto SiO_2 substrates patterned with holes. In both suspended and substrate-supported samples, a complex blend of low energy photoluminescence emissions are detected. The power and temperature dependence of these emissions, combined with Raman scattering information on the vibrational modes, suggest that the low energy emissions are defect-assisted phonon replicas, consistent with previously reported works[10-13, 15]. More importantly, we observe multi-phonon emissions, with replicas up to the 6th order. The low-energy emissions are stronger and broader for samples transferred from the growth substrate, likely due to the larger amount of defects/residues from the transfer process. These findings highlight important material design strategies that can be utilized to control excitonic dynamics in 2D van der Waals layers and advance the engineering tools needed to develop future 2D optoelectronic devices.

2. Materials and Methods

We examine five different types of WS_2 samples: 1) CVD-grown monolayers on SiO_2 (referred to as-grown), 2) CVD-grown monolayers on hBN, 3) CVT-grown bulk crystals exfoliated and encapsulated on both sides with hBN, 4) CVD-grown monolayers transferred to a fresh SiO_2 substrate, and 5) CVD-grown monolayers transferred and suspended on holes that were pre-patterned in the SiO_2 substrate. A visual summary of the samples is in the Supplementary Information in Figure S1. This comprehensive selection of WS_2 materials and preparation methods allow us to examine samples with different defect densities (CVD-grown vs. CVT/exfoliated), as well as examine the role of substrates and their inhomogeneities, by comparing hBN, SiO_2, and suspended samples.

The CVD growth is performed at atmospheric pressure (APCVD). Details on the precursors and substrate preparations are outlined in the supplementary information. For WS_2 grown on top of hBN, the growth process is the same as the growth process for monolayer samples, with the main difference being the substrates for WS_2 on hBN growth will have hBN exfoliated onto them via mechanical exfoliation, and then rinsed under electronic grade acetone followed by IPA to remove any tape residue.

The chemical vapor deposition process begins with an anneal for 60 minutes at 120°C in an Argon environment with 500sccm flow rate. The sulfur boat is heated to 85°C throughout the anneal. Following the anneal, the temperature of the furnace is ramped up from 120°C to 750°C in 40 minutes and from 750°C to 850°C in 10 minutes. The Argon flow rate is maintained at 200sccm from 120°C to 750° C and at 70sccm from 750°C to 850°C, and throughout the growth phase. The temperature of the sulfur boat is increased from 85°C to 175°C throughout the temperature ramp phase in the heating profile. The Hydrogen flow rate is ramped from 0 to 10sccm at 750°C and maintained at this rate until the end of the growth phase. Once the WO_3 boat reaches 750°C, the sulfur temperature should be at 175°C. At the end of the growth phase, the Hydrogen gas flow is turned off, the Argon flow rate is increased to 1000sccm to flush out any residual by-products of the chemical reaction and the sulfur and furnace heating elements are turned off. The Argon gas flow is turned off once the furnace cools down below 200°C.

For samples transferred from the growth substrate to a substrate patterned with holes, we used a water-assisted delamination process with polystyrene as a carrier layer [17]. Details on the transfer process are also included in the supplementary information.

Optical measurements from room temperature to 78 K were performed under high vacuum conditions, at 1.0×10^{-6} Torr, with a WITec Alpha 300RA system using the 532 nm line. The spectra were measured in the backscattering configuration using a 63× objective and an 1800 or 600 grooves mm^{-1} grating. The cooling was achieved with a Super-VariTemp Janis Research cryostat, using a continuous flow of liquid nitrogen as the cooling agent. This cryostat was adapted for Raman spectroscopy.

For temperatures below 78 K, we used a Montana Instrument cryostation equipped with a 100x objective in its chamber (Cryo-Optic) for high contrast imaging. The photoluminescence spectra were obtained by a single grating spectrometer (Horiba) and imaged on a CCD camera (Symphony I Horiba). For laser sources, we employed a 532 nm diode and tunable M-squared laser (515 to 680 nm).

3. Results

Optical excitation of WS_2 comprises free charge carriers, neutral excitons (bright and dark), charged trions (bright and dark), as well as lattice vibrations (phonons). In the presence of free carriers, an exciton can undergo an electron exchange scattering event or bind a free carrier forming a trion [6, 18-23]. Excitons and trions can interact with defects either by binding to a defect state or by elastic-scattering. The brightened dark excitons and their phonon replicas yield radiation emission and give rise to an extremely rich photoluminescence spectrum.

Figure 1a) shows the photoluminescence (PL) emission spectra from the five different samples at room temperature. The spectra are qualitatively similar for all of the samples, showing broad emissions in the same energy range. Notably, emissions can be better resolved in the spectrum collected from CVT WS_2 on hBN, revealing more than one peak. This is expected, since cleaner materials and substrates with fewer defects and inhomogeneities lead to narrow emission linewidths, consistent with previous reports [6, 8, 24].

Figure 1b shows the PL spectra for the same samples at T = 78K. These low-temperature spectra reveal a dramatic change relative to the room temperature emissions. The appearance of new peaks, the richer complexity of excitonic emissions, and the systematic variations between different samples point to interesting phonon- and defect-mediated processes. As discussed in previous work [13], at low temperature free excitons decay into lower-energy spin or momentum forbidden states, resulting in a relative decrease of the bright exciton peak and a relative increase of the low-energy dark exciton emissions. To help elucidate the specific origin of the PL emissions, we use electrostatic doping to modulate the charge carrier density. We used e-beam lithography and e-beam evaporation to pattern a gold contact on a CVD-grown WS_2 monolayer that had been transferred to a doped silicon substrate covered with a SiO_2 dielectric layer. The doped silicon was used as a back gate.

Since our CVD-grown WS_2 is electron doped, a negative gate voltage depletes the excess electrons and enhances the neutral excitations. Figure 1c) shows the photoluminescence spectra of WS_2 on SiO_2 at 78K at gate voltages ranging from +60 to -60 V, with 100uW illumination and laser photon energy of 2.33 eV. We note that the curve corresponding to Vg = 0 in Figure 1 c) shows a prominent peak above 2.0 eV, in addition to the broad peak at about 1.9 eV that dominates the spectrum for the CVD sample transferred on SiO_2 in Figure 1 b). This is because the two spectra are measured with different incident power (the power is 10 times higher for the gated spectra in Figure 1 c)) and the relative peak height for different emissions strongly depends on the incident power, as it will be discussed later. The broader energy peak near 1.9 eV is prominent for samples transferred from the growth substrate and it has a very weak gate dependence. This peak is likely related to the presence of defects and residues from the transfer process, as outlined later in the discussion section. At negative gate voltages, the free exciton emission X_A emerges, with peak energy marked by the vertical line at about 2.1 eV.

Following the identification of the neutral exciton emission X_A, the remainder of the peaks can then be identified by using the band diagram in Figure 2. The conduction band splitting gives rise to a spin-forbidden dark exciton X_D^{KK} and momentum-forbidden dark exciton X_D^{-KK}. It has been reported that the momentum forbidden dark exciton X_D^{-KK} lies about 10meV higher than that of the spin forbidden, due to exchange effects [6]. In figure 1c) emissions corresponding to these transitions can be identified at approximately 50 meV below X_A, where the spectrum shows a shoulder. As expected for neutral excitons, this feature increases with the applied negative gate voltage, like X_A (see also Figure S2). We labeled this transition as X_D^{KK}, although due to the close spacing between X_D^{KK} and X_D^{-KK} it is not possible to discern whether either transitions or both are contributing to this emission. The next prominent peak in 1c) has a gate dependence characteristic of negatively charged trions. This emission is ~76meV below X_A. This energy spacing from X_A is much larger than the ~20-35meV additional binding energy of an extra electron expected for bright trions T^- [8, 15, 16, 20-23], suggesting that the peak in Figure 1 c) is likely due to a negatively charged dark trion, indicated as T_D^{KK} in Figure 2. In fact, T_D^{KK} requires the additional binding energy corresponding to the splitting of the conduction band, energetically in agreement with the interpretation from magneto PL measurements in previous work [15].

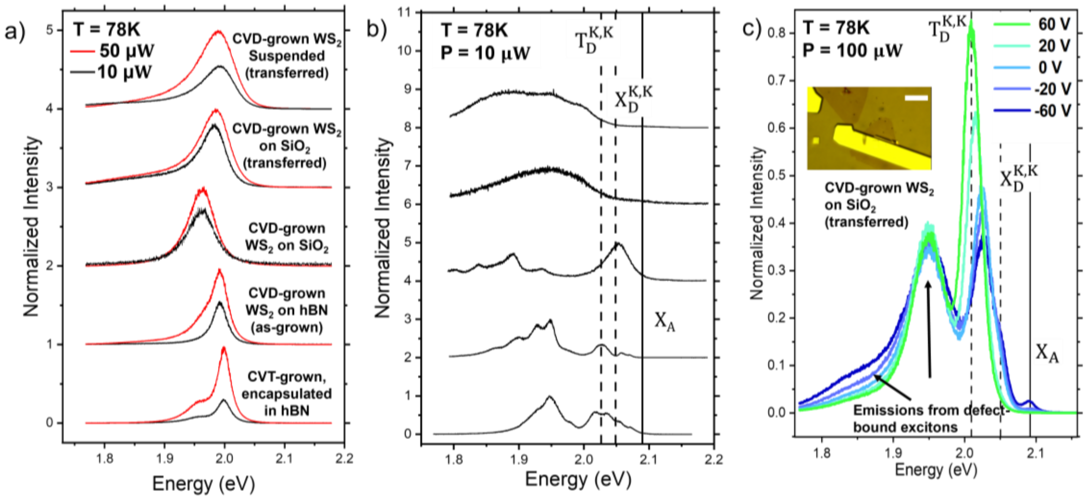

Figure 1. a) Room temperature PL of different types of WS_2 samples, namely (from top to bottom): CVD-grown WS_2 monolayers on SiO_2 transferred and suspended on top of pre-patterned holes on SiO_2; CVD-grown WS_2 monolayers transferred onto SiO_2; CVD-grown WS_2 monolayers on SiO_2; CVD-grown WS_2 monolayers on exfoliated hBN; CVT-grown bulk crystals exfoliated and encapsulated with hBN on both sides. b) PL of the same set of samples as in a) at 78K. c) Gated-PL spectra of transferred WS_2 on SiO_2 at 78K. The vertical lines mark the peaks corresponding to transitions specified in Figure 2 b). The inset shows an optical image of the gate sample. The scale bar is 20 µm.

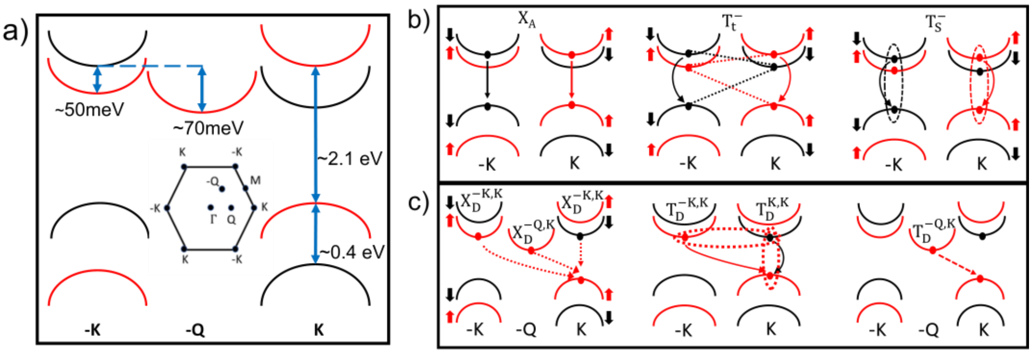

Figure 2. (a) Band alignment of WS_2 for high symmetry points in the first Brillouin zone. The energy spacings correspond to T = 78 K. b) Configurations of bright exciton and negatively charged trion (triplet and singlet) c) Configurations of dark (spin and momentum forbidden transitions) excitons and trions.

To better analyze the rich features of the lower energy spectra, Figure 3 shows a detailed analysis of the spectrum for the WS_2 sample grown on hBN by CVD. The two PL spectra in Fig. 3 c) are from the same flake, measured at two different locations. Although the low energy peaks can be found in all the samples, their intensity depends on the specific sample location. This is an example of the spectral emission variability within each flake that is also illustrated in the photoluminescence map in Fig. S3. The spatial inhomogeneity confirms that these peaks are related to the presence of defects in the materials and may be stronger in regions with higher defect densities.

In Figure 3 c), by marking the emission from the neutral excitons X_A, we can clearly measure the energy spacing of the other emissions relative to X_A. We note that the peaks corresponding to X_A (2.1 eV) and the bright trions T_- (2.068 eV) are the weakest peaks, while the low-energy emissions dominate the spectrum. Several recent studies have attributed these low-energy emissions to the brightening of dark excitons [6-8, 16, 19, 25-27], but clearly identifying the corresponding transitions and their brightening mechanism are challenging tasks, often leaving behind open questions. For the different types of samples described here, we already described above how we identify the zero-phonon lines of dark transitions X_D^{KK} and T_D^{KK}. As mentioned in the discussion of the spectra in Figure 1, X_D^{KK} is spaced from X_A by 50 meV, approximately the conduction band splitting, consistent with the zero-phonon line of the spin-forbidden dark exciton brightened by elastic scattering with defects. This vertical transition can also be brightened by a Γ phonon via spin-flip scattering. For WS_2 this is the Γ^5 phonon, corresponding to the in-plane out-of-phase oscillation of the chalcogen atoms with an energy of about 38 meV [28]. The emissions marked by the vertical orange lines correspond to peak energies matching the first and the third order phonon replicas for these phonon-brightened transitions in the lower and upper spectrum, respectively.

Similarly, we can identify the zero-phonon line of the momentum-forbidden transitions X_D^{-QK} (marked by a dotted line just above 2.025 eV) between electrons and holes in -Q and K bands, respectively. The energy spacing of this peak from X_A matches the spacing of the conduction band edges at -Q and K, about 70 meV, indicating that the brightening of the X_D^{-QK} zero-phonon line is due to elastic scattering with defects. These transitions can also be brightened by scattering with phonons carrying the matching momentum difference between the electron and the hole. These are acoustic phonons at the M point of the Brillouin zone that have been shown to strongly couple to excitonic transitions from previous experiments using resonant Raman spectroscopy [13]. In our spectra we can clearly see peaks with spacing of 28 meV matching the A1′(M)-LA(M) phonon for WS_2. Notably, the spacing of the peaks from the zero-phonon line indicates that we can measure up to the 6th order phonon replica for this phonon-brightened emission, as indicated by the purple dotted lines. Momentum conservation requires either just one phonon or an odd number of phonons that includes pairs of phonons with opposite momentum. The presence of replicas corresponding to an even number of phonons indicates that elastic scattering with defects must contribute to these emissions to conserve momentum. This is consistent with the spatial non-uniformity of the intensity of these low-energy emissions. It is also interesting to note that there are regions of the spectra where several different emissions are closely spaced. For example, in the spectrum corresponding to location 2 in Figure 3 c), the peaks from the first Γ^5 replica of X_D^{KK}, from the zero-phonon line X_D^{-QK} and from the dark trion T_D^{KK} are all located in the region of the spectrum where the emission is strongest, at 2.02 eV.

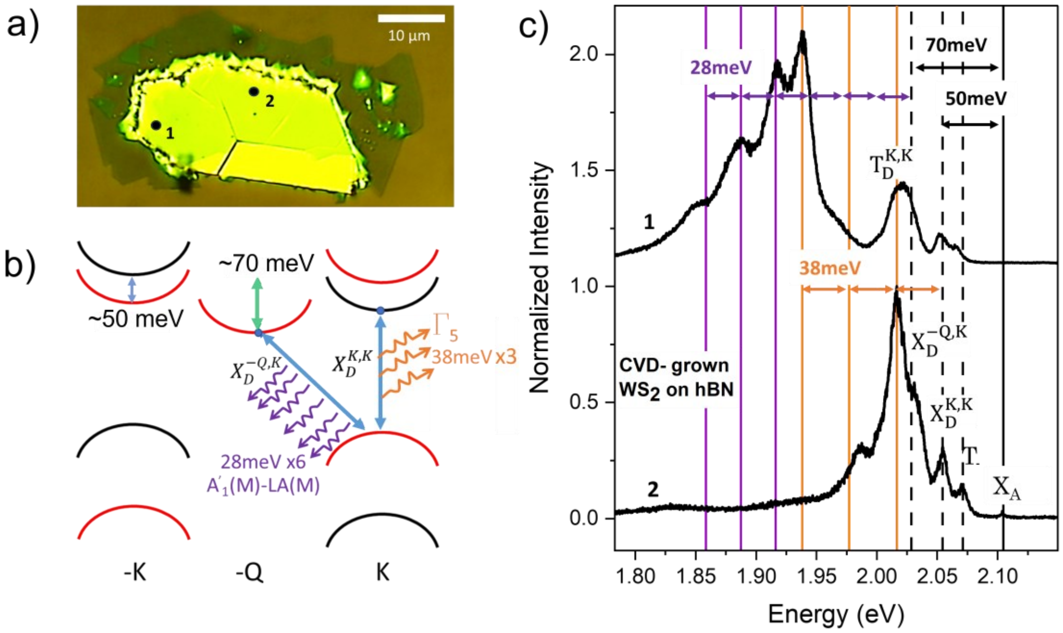

Figure 3. a) Optical image of the WS_2 flake grown on hBN (yellow) and SiO_2 (brown). The dots labeled as 1 and 2 indicate the positions where the spectra in c) were measured. b) Band diagram showing phonon replicas corresponding to emissions in c). The vertical transitions are spin forbidden and brightened by three Γ_5 phonons. The corresponding peak position in c) is marked by the orange line. The momentum indirect transition correspond to three peaks marked by the blue lines with three, four and five A'_1(m)-LA(M) phonons, respectively. c) Spectra measured at two different points for the flake shown in a), with 10 µW of incident power (532nm) at 78K. The top graph is one of the spectra in Figure 1 b).

Polarization dependence of the PL spectrum is a strong tool to study the character of emissions and their origins. Figure 4 a) shows the co- and cross-polarized spectra from the different WS_2 samples at 4K. For the suspended samples and the samples on the SiO_2 substrates, the emission is characterized by a broad peak as a background to sharper emissions. The broad peak is less prominent for the sample on hBN. While the broad peak is polarization independent, the sharper emission peaks do change with polarization, as expected for bright excitons and dark excitons that are not bound to defects. The lack of polarization dependence of the broad background peak suggests that its origin might be from excitons bound to defects, rather than excitons scattered by defects [29-34]. The sharper peaks can be more clearly distinguished in spectra with higher power in Figure 4 b), where vertical lines are used to identify the zero phonon lines and the corresponding replicas for the more prominent peaks, although small shoulders between the peaks reveal the presence of other emissions with smaller intensity, such as the zero-phonon line T_D^{KK}. The peaks identified at energy lower than the zero-phonon line X_D^{-QK} are replicas with spacings of about 22 meV, corresponding to the LA(M) phonon mode [13] and 28 meV, corresponding to the A_1'(M)-LA(M) phonon energy[28].

Figure 4 b) clearly shows that the relative peak height from different emissions changes as a function of power. Specifically, the peak heights of the zero-phonon lines and the phonon replicas continue to grow with power approximately linearly, while the broad defect background saturates. These results indicate that the broad background is due to defect-bound excitons, with emissions that are expected to saturate with power for a finite defect density, once all the defect traps are occupied by excitons. On the other hand, the zero-phonon lines and the phonon replicas for dark emissions are brightened by elastic scattering of excitons with defects, therefore the peak height continues to increase with increasing incident power.

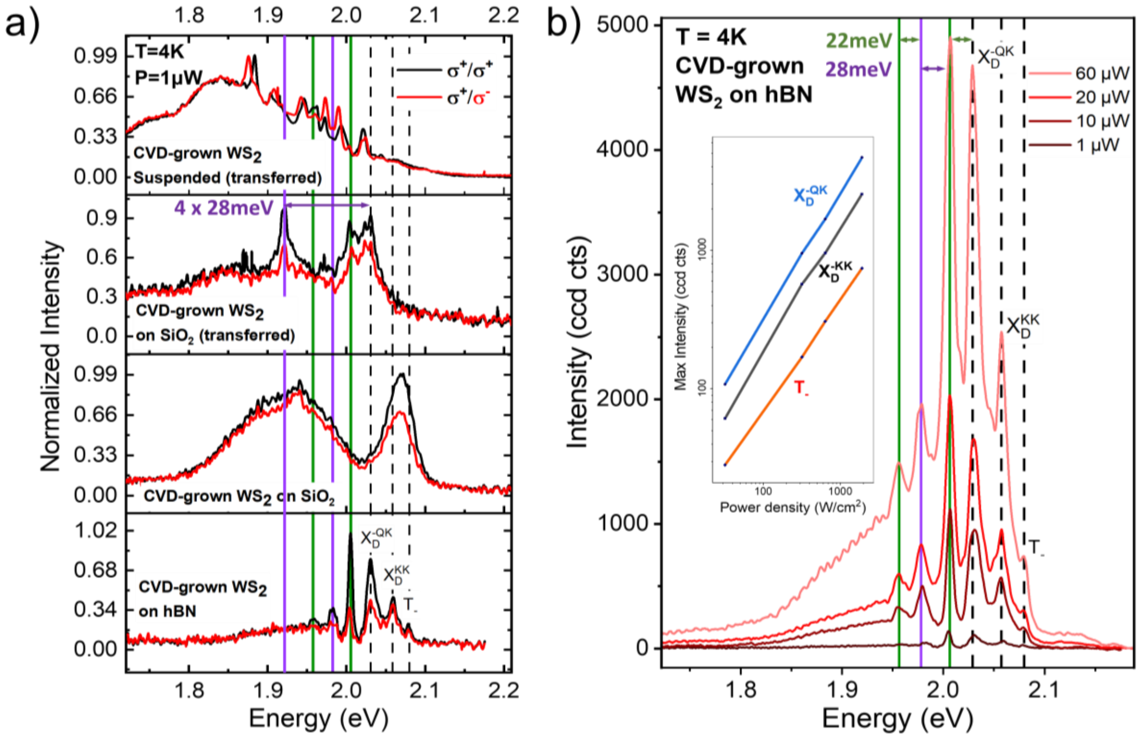

Figure 4 a) Helicity-resolved PL spectra taken at 4K from various WS_2 monolayer samples. b) PL emissions at various powers under unpolarized excitation laser.

4. Discussion

The low energy features in the photoluminescence spectra of all the different samples studied here show clear common features. They develop at low temperature and they dominate the spectrum at low incident laser power. This is evident from the maps of the PL spectra. At room temperature, where the emission is typically dominated by the bright emissions, i.e. by the trion peak (for CVD-grown material, typically electron-doped due to sulfur vacancies), the emission is spatially very uniform. At low temperature, the spatial non-uniformity emerges and the low-energy emissions are stronger in some regions of the flakes, as shown, for example, by the two spectra in Figure 3c) (see also photoluminescence maps in the supplementary information). We use the analysis of the spectra from different types of samples combined with the studies of the spectra as a function of electrostatic gating to identify the low energy emissions of dark excitations either as zero phonon lines or as their related phonon replicas. The spatial non-uniformity of the spectrum points to the essential role played by defects in the brightening process. Since the zero-phonon lines match the energy spacing from the neutral exciton emission X_A that is expected from the corresponding dark transition in the WS_2 band diagram (see Figure 2), the defect-assisted brightening must be the result of elastic scattering, rather than emissions from excitons bound to defects observed in previous works, where the energies of the low-energy emission zero phonon lines were determined by the defect binding energies [11]. In addition, we can clearly identify peaks from phonon replicas of the zero-phonon lines by matching their spacing to WS_2 phonons that satisfy the energy and momentum requirements to brighten these dark transitions. For the brightening of momentum-indirect dark transitions, we identify zone-edge M phonons that yield emissions up to 6th order replicas of the corresponding zero-phonon line. This result is consistent with previous observations of strong exciton-phonon scattering intensity for M phonons in WS_2 [13]. Our work elucidates that this exciton-phonon coupling is not strongly affected by the substrate, since these low-energy multi-phonon replicas can be identified in samples with SiO_2 and hBN substrates, as well as in suspended samples, as shown in Fig. 4a). It is interesting to note that in semiconductors the intensity of phonon replicas with multi-phonon emission can be related to the electron-phonon coupling via the Huang-Rhys factor [35-37]. Although this work is mainly focused on identifying the phonon replicas and their occurrence for different types of samples, in future work we plan to study the intensities of the phonon replicas for different transitions and different phonon modes to extract Huang-Rhys factors for WS_2 and other transition metal dichalcogenides.

By comparing the spectra from different types of samples, we find that the effect of the substrate and the defect density in the WS_2 is mainly in the broadening of these emissions. As expected, more uniform substrates and low- defect density samples yield sharper emission lines. The broader low-energy emissions are measured from the transferred samples (see for example transferred CVD WS_2 in Figure 1b)), indicating higher defect density from residues related to the transfer process. However, measurements at lower temperature in Figure 4, show that sharp phonon replicas emerge from the broad emission background, confirming that phonon replicas are present also in the transferred samples. While the phonon replicas and the zero-phonon lines are polarization-dependent and indicate brightening of dark excitons that is assisted by elastic scattering with defects, the broad polarization-independent background is indicative of excitons bound to defects. Unlike emissions brightened by elastic scattering, emissions from excitons bound to defects saturate with increasing power, as shown in Figure 4 b).

5. Conclusions

In summary, we show that the low-energy emissions in monolayer WS_2 are largely governed by scattering with phonons and elastic scattering from defects, which remain regardless of the substrate or growth conditions. In addition, the power dependence and the spatial non-uniformity confirm that defects seem to play a key role in the occurrence of radiative recombination from dark excitons. However, these defects are not related to the substrate or different defect densities from different growth processes, since these low energy emissions are ubiquitous for samples on different substrates, grown and prepared with different methods. In our analysis, evidence of emissions due to defect-bound exciton described in previous work [11] was limited to a broad background signal that was prominent in samples with residues from the transfer process. Our findings highlight important physics and material design strategies that can be utilized to control excitonic dynamics in 2D van der Waals layers and advance the engineering tools needed for development of 2D optoelectronic devices.

Supplementary Materials: The following supporting information can be downloaded at: www.mdpi.com/xxx/s1, Figure S1: title; Table S1: title; Video S1: title.

Author Contributions: Conceptualization, ERA, PB, SN, EVK; methodology, ERA, TL, IB; validation, ERA; formal analysis, ERA, PB; investigation, ERA, IB, TL; resources, TL, RB, YH, DR ; data curation, ERA.; writing—original draft preparation, ERA, PB; writing—review and editing, all authors; visualization, ERA; supervision, PB, SN, EVK; project administration, PB, SN, EVK; funding acquisition, PB, EVK, SN. All authors have read and agreed to the published version of the manuscript.” Please turn to the CRediT taxonomy for the term explanation. Authorship must be limited to those who have contributed substantially to the work reported.

Funding: This research was funded by NSF ECCS, grant number 2132098.

Data Availability Statement: Supporting data will be shared upon request.

Acknowledgments:

Conflicts of Interest: The authors declare no conflict of interest.

References

[1] G. Wang *et al.*, "Colloquium: Excitons in atomically thin transition metal dichalcogenides," *Reviews of Modern Physics,* vol. 90, no. 2, Apr 2018, Art no. 021001, doi: 10.1103/RevModPhys.90.021001.

[2] K. F. Mak, K. L. He, J. Shan, and T. F. Heinz, "Control of valley polarization in monolayer MoS2 by optical helicity," *Nature Nanotechnology,* vol. 7, no. 8, pp. 494-498, Aug 2012, doi: 10.1038/nnano.2012.96.

[3] Y. P. Liu, Y. J. Gao, S. Y. Zhang, J. He, J. Yu, and Z. W. Liu, "Valleytronics in transition metal dichalcogenides materials," *Nano Research,* vol. 12, no. 11, pp. 2695-2711, Nov 2019, doi: 10.1007/s12274-019-2497-2.

[4] J. R. Schaibley *et al.*, "Valleytronics in 2D materials," *Nature Reviews Materials,* vol. 1, no. 11, Nov 2016, Art no. 16055, doi: 10.1038/natrevmats.2016.55.

[5] K. F. Mak, D. Xiao, and J. Shan, "Light-valley interactions in 2D semiconductors," *Nature Photonics,* vol. 12, no. 8, pp. 451-460, Aug 2018, doi: 10.1038/s41566-018-0204-6.

[6] P. Li *et al.*, "Intervalley electron-hole exchange interaction and impurity-assisted recombination of indirect excitons in WS2 and WSe2 monolayers," *Physical Review B,* vol. 106, no. 8, 2022/8// 2022, doi: 10.1103/PhysRevB.106.085414.

[7] H. Dery and Y. Song, "Polarization analysis of excitons in monolayer and bilayer transition-metal dichalcogenides," *Physical Review B - Condensed Matter and Materials Physics,* vol. 92, no. 12, 2015/9// 2015, doi: 10.1103/PhysRevB.92.125431.

[8] M. Yang *et al.*, "Relaxation and darkening of excitonic complexes in electrostatically doped monolayer Formula Presented: Roles of exciton-electron and trion-electron interactions," *Physical Review B,* vol. 105, no. 8, 2022/2// 2022, doi: 10.1103/PhysRevB.105.085302.

[9] Y. Song and H. Dery, "Transport theory of monolayer transition-metal dichalcogenides through symmetry," *Physical review letters,* vol. 111, no. 2, p. 026601, 2013.

[10] S. Brem *et al.*, "Phonon-Assisted Photoluminescence from Indirect Excitons in Monolayers of Transition-Metal Dichalcogenides," *Nano Letters,* vol. 20, no. 4, pp. 2849-2856, Apr 2020, doi: 10.1021/acs.nanolett.0c00633.

[11] P. Rivera *et al.*, "Intrinsic donor-bound excitons in ultraclean monolayer semiconductors," *Nature Communications,* vol. 12, no. 1, Feb 2021, Art no. 871, doi: 10.1038/s41467-021-21158-8.

[12] M. H. He *et al.*, "Valley phonons and exciton complexes in a monolayer semiconductor," *Nature Communications,* vol. 11, no. 1, Jan 2020, doi: 10.1038/s41467-020-14472-0.

[13] D. Bao, A. G. del Aguila, T. T. H. Do, S. Liu, J. J. Pei, and Q. H. Xiong, "Probing momentum-indirect excitons by near-resonance photoluminescence excitation spectroscopy in WS2 monolayer," *2d Materials,* vol. 7, no. 3, Jul 2020, Art no. 031002, doi: 10.1088/2053-1583/ab817a.

[14] M. Grundmann, *The Physics of Semiconductors*, 3 ed.: Springer Cham, 2015.

[15] M. Zinkiewicz *et al.*, "Excitonic Complexes in n-Doped WS2 Monolayer," *Nano Letters,* vol. 21, no. 6, pp. 2519-2525, Mar 2021, doi: 10.1021/acs.nanolett.0c05021.

[16] L. P. McDonnell, C. C. Huang, Q. Cui, D. W. Hewak, and D. C. Smith, "Probing Excitons, Trions, and Dark Excitons in Monolayer WS2 Using Resonance Raman Spectroscopy," *Nano Letters,* vol. 18, no. 2, pp. 1428-1434, 2018/2// 2018, doi: 10.1021/acs.nanolett.7b05184.

[17] A. Gurarslan *et al.*, "Surface-energy-assisted perfect transfer of centimeter-scale monolayer and few-layer MoS2 films onto arbitrary substrates," *ACS nano,* vol. 8, no. 11, pp. 11522-11528, 2014.

[18] J. S. Ross *et al.*, "Electrical control of neutral and charged excitons in a monolayer semiconductor," *Nature Communications,* vol. 4, 2013, doi: 10.1038/ncomms2498.

[19] M. Zinkiewicz *et al.*, "Excitonic Complexes in n-Doped WS2Monolayer," *Nano Letters,* vol. 21, no. 6, pp. 2519-2525, 2021/3// 2021, doi: 10.1021/acs.nanolett.0c05021.

[20] D. Vaclavkova *et al.*, "Singlet and triplet trions in WS2 monolayer encapsulated in hexagonal boron nitride," *Nanotechnology,* vol. 29, no. 32, 2018/6// 2018, doi: 10.1088/1361-6528/aac65c.

[21] T. C. Berkelbach, M. S. Hybertsen, and D. R. Reichman, "Theory of neutral and charged excitons in monolayer transition metal dichalcogenides," *Physical Review B,* vol. 88, no. 4, Jul 2013, Art no. 045318, doi: 10.1103/PhysRevB.88.045318.

[22] G. Plechinger *et al.*, "Trion fine structure and coupled spin-valley dynamics in monolayer tungsten disulfide," *Nature Communications,* vol. 7, 2016/9// 2016, doi: 10.1038/ncomms12715.

[23] P. Techniki *et al.*, "Valley polarization of singlet and triplet trions in WS 2 monolayer in magnetic fields," in "Journal: Physical Chemistry Chemical Physics."

[24] P. Rivera *et al.*, "Intrinsic donor-bound excitons in ultraclean monolayer semiconductors," *Nature Communications,* vol. 12, no. 1, 2021/12// 2021, doi: 10.1038/s41467-021-21158-8.

[25] M. He *et al.*, "Valley phonons and exciton complexes in a monolayer semiconductor," *Nature Communications,* vol. 11, no. 1, 2020/12// 2020, doi: 10.1038/s41467-020-14472-0.

[26] M. Selig, G. Berghauser, M. Richter, R. Bratschitsch, A. Knorr, and E. Malic, "Dark and bright exciton formation, thermalization, and photoluminescence in monolayer transition metal dichalcogenides," *2d Materials,* vol. 5, no. 3, Jul 2018, Art no. 035017, doi: 10.1088/2053-1583/aabea3.

[27] M. Zinkiewicz *et al.*, "Neutral and charged dark excitons in monolayer WS 2 Neutral and charged dark excitons in monolayer WS 2 †."

[28] A. Berkdemir *et al.*, "Identification of individual and few layers of WS2 using Raman Spectroscopy," *Scientific reports,* vol. 3, no. 1, p. 1755, 2013.

[29] M. Zhou, W. Wang, J. Lu, and Z. Ni, "How defects influence the photoluminescence of TMDCs," in *Nano Research* vol. 14, ed: Tsinghua University, 2021, pp. 29-39.

[30] K. Greben, S. Arora, M. G. Harats, and K. I. Bolotin, "Intrinsic and Extrinsic Defect-Related Excitons in TMDCs," *Nano Letters,* vol. 20, no. 4, pp. 2544-2550, 2020, doi: 10.1021/acs.nanolett.9b05323.

[31] R. Sharma, "Spectroscopic correlation of chalcogen defects in atomically thin Journal of Physics : Materials Spectroscopic correlation of chalcogen defects in atomically thin," vol. 2, 2020.

[32] M. Zhou, W. Wang, J. Lu, and Z. Ni, "How defects influence the photoluminescence of TMDCs," *Nano Research,* vol. 12, no. 1, 2020, doi: 10.1007/s12274-020-3037-9.

[33] V. Carozo *et al.*, "Optical identification of sulfur vacancies: Bound excitons at the edges of monolayer tungsten disulfide," *Science Advances,* vol. 3, no. 4, pp. 1-10, 2017, doi: 10.1126/sciadv.1602813.

[34] Z. Wu and Z. Ni, "Spectroscopic investigation of defects in two-dimensional materials," *Nanophotonics,* vol. 6, no. 6, pp. 1219-1237, 2017, doi: 10.1515/nanoph-2016-0151.

[35] K. Huang and A. Rhys, "Theory of light absorption and non-radiative transitions in F-centres," *Proceedings of the Royal Society of London,* vol. 204, Series A, p. 18, 1950.

[36] M. Lax, "CITATION CLASSIC - THE FRANCK-CONDON PRINCIPLE AND ITS APPLICATION TO CRYSTALS," *Current Contents/Physical Chemical & Earth Sciences,* no. 38, pp. 16-16, 1985.

[37] M. Grundmann, *The Physics of Semiconductors*, Third ed. (Graduate Texts in Physics). Springer International Publishing, 2016.